Morphology and surface reactivity relationship in the Li1+xMn2–xO4 spinel with x = 0.05 and 0.10: a combined first-principle and experimental study

Ambroise Quesne-Turin, Germain Vallverdu, Delphine Flahaut, Joachim Allouche, Laurence Croguennec, Michel Ménétrier, Isabelle Baraille

Morphology and surface reactivity relationship in the $Li_{1+x}Mn_{2-x}O_4$ spinel with x = 0.05 and 0.10: A combined first-principle and experimental study

Ambroise Quesne-Turin[1,2,3], Germain Vallverdu[1,3], Delphine Flahaut[1,3], Joachim Allouche[1], Laurence Croguennec[2,3], Michel Ménétrier[2,3] and Isabelle Baraille[1,3].*

[1]CNRS/ Univ Pau & Pays Adour, Institut des Sciences Analytiques et de Physico-chimie pour l'Environnement et les Matériaux, UMR5254, 64000, Pau, France

[2] CNRS, Univ. Bordeaux, Bordeaux INP, ICMCB UPR 9048, F-33600 Pessac, France

[3] RS2E, Réseau Français sur le Stockage Electrochimique de l'Energie, FR CNRS 3459, F-80039 Amiens Cedex 1, France

Corresponding Author

*Germain Vallverdu

germain.vallverdu@univ-pau.fr

KEYWORDS

Surface reactivity, XPS, spinel positive electrode materials, stoichiometry, first-principle calculations

ABSTRACT

This paper focuses on the surface reactivity of two spinel samples with different stoichiometries and crystal morphologies, namely $Li_{1+x}Mn_{2-x}O_4$ with x = 0.05 and x =0.10. $LiMn_2O_4$ compounds are good candidates as positive electrode of high power lithium-ion batteries for portable devices. The samples were investigated using both experimental and theoretical approaches. On the experimental point of view there were characterized in depth from XRD, SEM and XPS analyses. Then the reactivity was investigated through the adsorption of (SO_2) gaseous probes, in controlled conditions, followed by XPS characterization. First-principle calculations were conducted simultaneously in order to investigate the electronic properties and the reactivity of relevant surfaces of an ideal $LiMn_2O_4$ material. The results allow us to conclude that the reactivity of the samples is dominated by an acido-basic reactivity and the formation of sulfite species. Nonetheless, on the x = 0.05 sample, both sulfite and sulfate species are obtained, the later, in lesser extent, corresponding to a redox reactivity. Combining, experimental and theoretical results, this redox reactivity could be associated to the presence of a larger quantity of Mn^{4+} cations on the last surface layers of the material linked to a specific surface orientation.

1. INTRODUCTION

The $LiMn_2O_4$ spinel material is a good candidate at the positive electrode of high power lithium-ion batteries for portable devices. Its theoretical capacity is approximately 140 $mAh.g^{-1}$,[1] as much as $LiCoO_2$, still the most commonly used positive electrode of commercialized lithium-ion batteries[2]. Contrary to $LiCoO_2$, $LiMn_2O_4$ is considered as a non-toxic and low cost material with an operating voltage of 4.1 V vs. Li^+/Li. The key issue for $LiMn_2O_4$ is a fast capacity fading upon cycling or storage at a temperature higher than 50°C, which is especially in relationship with the transition metal dissolution into the electrolyte[3,4]. It is this latter key issue that we want to address by considering the specific reactivity of different surfaces of the spinel structure. As the electrolyte contains different alkyl carbonates as solvents and a Li salt (for instance $LiPF_6$), different reactions can occur with $LiMn_2O_4$. Dissolution of manganese in the electrolyte ($2\ Mn^{3+}_{(solid)} \rightarrow Mn^{4+}_{(solid)} + Mn^{2+}_{(solution)}$) has been significantly observed for $LiMn_2O_4$ [5,6]. In order to circumvent this issue, the use of an alternative electrolyte, such as $LiB(C_2O_4)_2$ [4], or manganese and oxygen atoms substitutions by aluminum and fluorine atoms[3], respectively, was considered and lead to an improvement of cycling properties at high temperature. Even if more limited, the $LiMO_2$ layered oxides (M = Mn, Ni, Co) suffer also from transition metal dissolution. To improve their electrochemical performance at high potential, the formation of a coating with Al_2O_3 for example has been revealed as a fruitful method to modify the surface reactivity of the material toward the electrolyte. Previously, we studied on the basis of XPS analysis and first-principal calculations, the surface reactivity of $LiCoO_2$ and NMC materials and the effect of a Al_2O_3 coating[7–9] versus gaseous probes. We evidenced that the amount of adsorbed species and their adsorption mode (redox and/or acid/base) are governed by the nature of the transition metal of the electrode material. Moreover, the Al_2O_3 coating of those electrode materials results in both

decreasing the active site concentration and modifying the adsorption mode of the gaseous probe. For $LiCoO_2$, the coating modifies the surface reactivity with the identification of both sulfate and sulfite species, which is in line with a change in the adsorption mode from redox toward acid–base after Al/Co substitution[10]. In the case of NMC materials, the phenomenon is more complex related to the cation mixing effect.

In this paper, we studied the surface reactivity of $Li_{1+x}Mn_{2-x}O_4$ (x = 0.05 and 010) spinel materials showing different stoichiometry and morphology. We performed the adsorption of a gaseous probe (SO_2) on the materials, in controlled conditions and used both XPS analyses and first-principle calculations to identify the adsorption mode of SO_2 on the surface and characterize its reactivity. We also determined the nature of the active sites on the material surface and quantify their concentration.

2. MATERIALS AND METHODS

2.1. The two samples $Li_{1+x}Mn_{2-x}O_4$ (x = 0.05, 0.10)

Two samples of $Li_{1+x}Mn_{2-x}O_4$ were prepared for x = 0.05 and 0.10 according to the method described in details by Masquelier *et. al.*[11], *i.e.* by mixing Li_2CO_3 and MnO(OH) in stoichiometric amounts according to the target composition and by heating the obtained mixture at 400 °C for 2 h and at 800 °C for 20 h in air. An intermediate grinding was performed and the powder was cooled down at 10 °C/min. As described in details in reference 12 the two spinel materials crystallize in the cubic $Fd\bar{3}m$ space group, the manganese ions occupying the *16d* octahedral sites of a cubic closed-packed oxygen (*32e* sites) array. The MnO_6 octahedra are linked to each other by sharing edges, forming a three-dimensional framework (Mn_2O_4)

containing channels where the lithium ions occupy *8a* tetrahedral sites. In the case of $Li_{1+x}Mn_{2-x}O_4$, a partial substitution of lithium for manganese is observed in the *16d* sites. The two samples were characterized in depth combining chemical analyses by inductively coupled plasma optical emission spectrometry, and structural analyses by X-ray and neutron diffraction as reported in reference 13. The more overlithiated the spinel phase $Li_{1+x}Mn_{2-x}O_4$, the smaller is the lattice parameter (8.2484(2) Å for $LiMn_2O_4$, 8.2307(4) Å for $Li_{1.05}Mn_{1.95}O_4$ and 8.2188(3) Å for $Li_{1.10}Mn_{1.90}O_4$), in good agreement with a higher average oxidation state for manganese (ionic radii of 0.58 Å for Mn^{3+} versus 0.53 Å for Mn^{4+})[14] as required for charge compensation of the lithium excess within the host structure. Indeed, $3Mn^{3+}$ ions are replaced in the *16d* sites by ($1Li^+ + 2Mn^{4+}$), with a general formula $Li_{1+x}Mn^{4+}_{1+2x}Mn^{3+}_{1-3x}O_4$. 44% and 37% of the manganese ions are thus expected to be Mn^{3+} in $Li_{1.05}Mn_{1.95}O_4$ and $Li_{1.10}Mn_{1.90}O_4$ respectively. Note that the specific areas of the two materials have been determined by a Micromeritic ASAP 2010, using the Brunauer–Emmett–Teller (BET) theory[15] and were found to be very similar, below 2 $m^2.g^{-1}$.

2.2.Scanning Electron Microscopy (SEM)

The surface morphology of the samples was analyzed using a JEOL JAMP 9500F Auger Nanoprobe microscope under Ultra High Vacuum conditions (< 2 $x10^{-9}$ mbar) fitted with a Schottky field emission electron gun, using a conventional secondary electron detector (SED) in the analysis chamber. The analyses were performed using a beam voltage of 30 keV and a beam current of 2 nA. The materials were gold-sputtered with a Denton Vacuum Desk V metalizer before being mounted on the sample holder.

2.3. Gas probe adsorption

The SO_2 adsorption was performed in a Micromeritic Autochem 2920 Analyzer. A first step dedicated to the cleaning of the powders surface was conducted in order to desorb all the physisorbed species. The $Li_{1+x}Mn_{2-x}O_4$ powders were introduced in the silica reactor, and then submitted to an argon flow at 350 °C for 4 h.

The powders were then maintained at 80 °C for 1 h under a Helium flow to ensure that the next step, gas probe adsorption, was performed on a stable surface. Finally, the adsorption of SO_2 at the surface of $Li_{1+x}Mn_{2-x}O_4$ was performed at 350 °C for 15 min under a gas flow (50 $mL \cdot min^{-1}$) containing 0.02% of SO_2 in helium. Samples were kept under a He flow at 80 °C to remove the physisorbed species from the samples surface. The gas probe adsorption has been performed three times for most samples to ensure the reproducibility of the experiment. After adsorption, the samples were transferred into a glove box before being analyzed, without being submitted to ambient atmosphere.

The choice of the SO_2 gaseous probe was based on the small molecule size and its acidic strength. The identification of adsorbed species as well as the involved mechanisms can be easily obtained by X-ray photoelectron spectroscopy by considering the large binding energy (B.E.) scale (almost 10 eV[16,17]) of the S 2p core peaks depending of the chemical environments. The SO_2 gaseous probe can be adsorbed on the surface, either according to basic/acidic and/or to redox mechanisms[7–10]. If the adsorption is driven by an acid/base mode, SO_3^{2-} sulfite species will be formed at the surface characterized by a B.E. of the S $2p_{3/2}$ core peak at ~167.5 eV. In case of redox adsorption mode, the adsorption will lead to the formation of SO_4^{2-} sulfate species characterized by a B.E. of the S $2p_{3/2}$ core peak at ~169.0 eV[18].

Quantitative information can also be obtained with the evaluation of the S/Mn atomic ratios, deduced from XPS analysis of the core peaks of the adsorbed molecules (S 2p for SO_2 gas probe) as well as the metals (Mn 2p for Mn) in the electrode material.

2.4. X-Ray Photoelectron Spectroscopy (XPS)

The XPS analyses were performed on a Kratos Axis Ultra spectrometer with a focused monochromatized Al Kα radiation. The applied current and voltage were of 12 mA and 12 kV respectively. The spot size was of 700x400 μm^2. The powders were placed on a Cu double tape fixed on the sample holder. The samples preparation, for XPS measurements, was performed in a glove box and transferred to the one which is directly connected to the XPS spectrometer. The pressure in the analysis chamber was ca. 5 x 10^{-9} mbar. The spectra were calibrated in B.E. scale from the Mn $2p_{3/2}$ peak of Mn^{4+} at 642.3 eV.

2.5. Theoretical calculation

Periodic Density Functional Theory (DFT) calculations were performed to estimate the relative stability of crystalline surfaces of the materials, to compute the adsorption energies of the gaseous probes and to investigate the underlying electronic processes. All calculations were performed with the Vienna Ab initio Simulation Package[19,20] (VASP). The wave-functions were described in the Projector Augmented Wave[21] (PAW) formalism using a plane waves basis set and a cut-off energy of 550 eV. All calculations were done using the GGA exchange and correlation functional of Perdew and Wang[22,23] (PW91). The Brillouin zone integration was done using a 4×4×4 or 4×4×1 k-points mesh uniformly distributed around the Γ point of the reciprocal space for bulk or surface systems respectively. $LiMn_2O_4$ is characterized by 3d electrons strongly

localized on the manganese atoms and requires to perform calculations using the DFT+U formalism. We used the implementation of the rotationally invariant approximation of Dudarev *et al*[24], where U and J are melted in a single U_{eff} = U - J parameter, and we adopted the value U_{eff} = 4.84 eV from the work of Xu *et al*[1]. All calculations were carried out considering spin polarization with ferromagnetic ordering. Charge calculations were performed by using Bader's topological analysis[25,26]. For bulk calculations, all degrees of freedom were fully relaxed whereas the cell shape and volume were kept fixed and only atomic positions of the first atomic layers were relaxed in the case of surface calculations.

We performed calculation on bulk and surface models of $LiMn_2O_4$ and analyzed the atomic charges and the magnetic moments, in particular, to determine the oxidation state of the manganese atoms. Calculations were performed in similar conditions for $Mn^{II}O$, $Mn^{III}{}_2O_3$ and $Mn^{IV}O_2$ as references to determine standard values for the Mn magnetic moments. They lead to 4.7, 4.0 and 3.4 μ_B for Mn^{2+}, Mn^{3+} and Mn^{4+} respectively. The details of these calculations are provided in Supporting Information, Table 1.

3. RESULTS

3.1. Bulk characterization

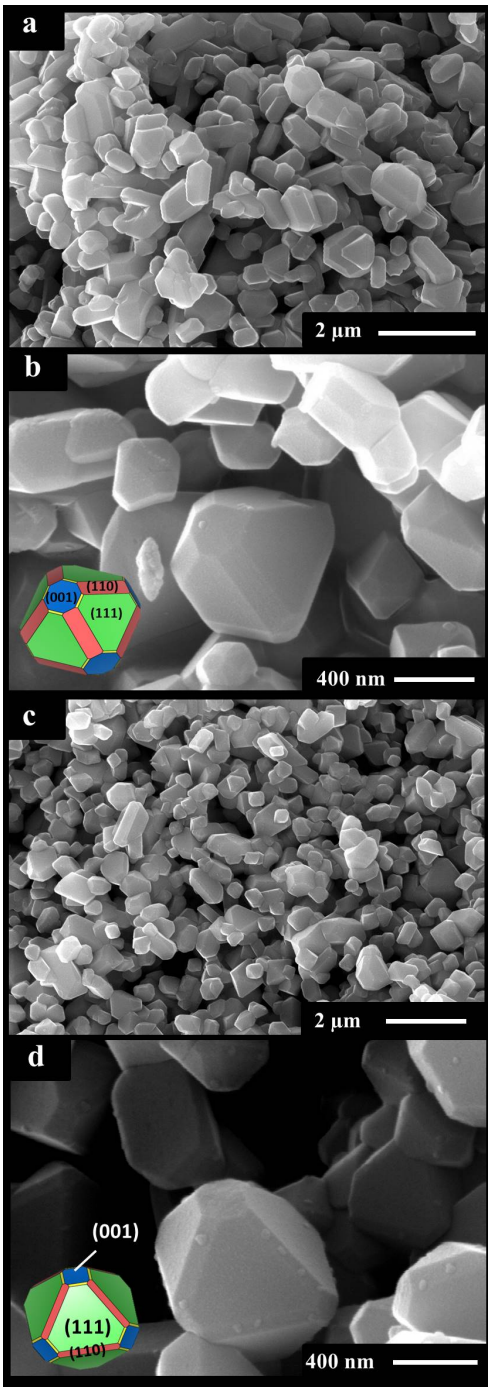

Figure 1. SEM images of $Li_{1+x}Mn_{2-x}O_4$. (a) and (b) for x = 0.05, (c) and (d) for x = 0.10. Insets in the b and d images give schematic representation of the central particles. The crystallographic faces are given with different colors depending on their orientation: green for (111), blue for (001), red for (110) and orange for (113).

The morphology of the materials was characterized by scanning electron microscopy. As displayed in the crystal sizes are in a range of 200-1000 nm. The $Li_{1.05}Mn_{1.95}O_4$ material, presented in Figure 1 a-b, exhibits truncated surfaces at the edges and vertexes of the octahedral crystals. On the basis of a previous work of Kim *et al*[27], the surface orientations can be assumed to correspond to the lattice planes (111), (001) and (110) which are commonly observed in the case of cubic lattices (see the graphical inset given in Figure 1 b). The crystal morphology appears similar for the $Li_{1.10}Mn_{1.90}O_4$ material. Nonetheless, on the crystal displayed on Figure 1 d, the (110) lattice plane appears in a lesser extent.

3.2.Surface characterization

XPS analyses have been performed on bare and adsorbed materials. The Mn 2p, Mn 3s, O 1s, Li 1s, S 2p and C 1s core peaks have been recorded to follow the evolution of the electronic structure of the materials after SO_2 adsorption and to identify the nature and the concentration of the adsorbed species.

3.2.1. Before SO_2 adsorption

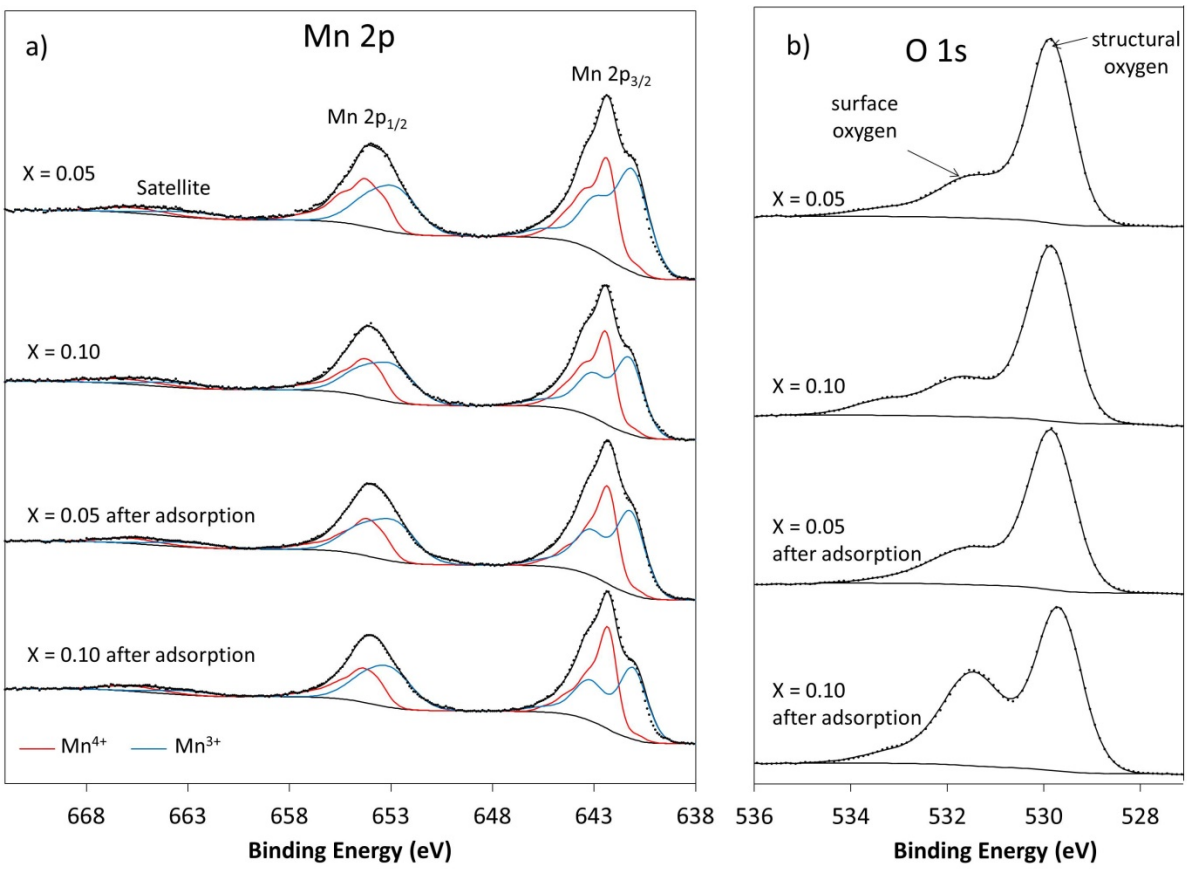

Figure 2. Mn 2p (a) and O 1s (b) core peaks for $Li_{1+x}Mn_{2-x}O_4$ materials with x = 0.05 and x = 0.10, before and after SO_2 adsorption. Blue and red curves correspond to the contributions of Mn^{3+} and Mn^{4+} species respectively, according to the reference materials (Figure S1).

	x = 0.05		x = 0.10	
	B.E. (eV)	**At. %**	**B.E. (eV)**	**At. %**
Mn $2p_{3/2}$	642.3	17.5	642.3	13.9
O 1s	529.9	26.7	529.9	22.1
	531.5	11.6	531.7	9.9
		38.3		32.0
C 1s	285.0	22.4	285.0	37.1
	286.5	6.3	286.4	5.4
	287.8	2.6	287.8	0.8
	288.9	1.6	289.0	3.2
		32.9		46.5
Li 1s	54.2	11.3	54.2	7.6

Table 1. Binding energies and atomic percentages determined from XPS analysis for $Li_{1+x}Mn_{2-x}O_4$ materials with x = 0.05 and 0.1.

The XPS Mn 2p spectra of the spinel materials are given before and after adsorption in Figure 2 a. They consist in the two main components Mn $2p_{3/2}$ and Mn $2p_{1/2}$, due to the spin orbit coupling, and satellites associated to those main peaks located at 11 eV toward the higher binding energy side. The satellite associated to the Mn $2p_{3/2}$ component is hidden by the Mn $2p_{1/2}$ component. The area ratio between the Mn $2p_{3/2}$ / Mn $2p_{1/2}$ is 2:1. The overall envelope of Mn $2p_{3/2}$ peak evidences two oxidation states for the manganese cations according to the shoulder observed for the at 641.4 eV. The Mn 2p spectra can be decomposed in two contributions due to the Mn^{3+} (641.4 eV) and Mn^{4+} (642.3 eV) cations. This identification of the mixed valency of the manganese cation at the surface is confirmed by the Mn 3s spectra (Figure S2). Actually, the exchange interaction of Mn 3s and 3d electrons leads to two photoemission final states and

therefore to a splitting of the Mn 3s peak in two components for which the B.E. splitting value is directly related to the Mn oxidation state. The B.E. splitting values for the $Li_{1+x}Mn_{2-x}O_4$ is 4.9 eV for x = 0.05 and 4.8 eV for x = 0.10. Those values intermediate between those reported for a pure Mn^{3+} and Mn^{4+} (4.5 eV and 5.5 eV[28] respectively) confirm the mixed valence state ($Mn^{3+/4+}$) as reported in the literature[29].

The ratio of Mn^{3+} and Mn^{4+} can be determined from the Mn 2p spectra of spinel materials. For this purpose, a decomposition of the Mn 2p peaks has been performed in an accurate manner described in Figure S1. We obtained roughly the same results for the two materials, 56 ± 1% and 54 ± 2% of Mn^{3+} species in the $Li_{1.05}Mn_{1.95}O_4$ and the $Li_{1.10}Mn_{1.90}O_4$ materials, respectively. It reveals - by comparison with the expected average content in Mn^{3+} within $Li_{1+x}Mn_{2-x}O_4$ (44% for x = 0.05 and 37% for x = 0.10) - that manganese ions are partially reduced at the surface of the spinel-type materials.

The O 1s spectra of the bare materials, given in Figure 2b, present two contributions, one at 529.7 eV associated to the oxygen anions of the materials, and a second one at 531.5 eV related to the under-coordinated oxygen anions from the surface[10]. The O 1s signal around 533 eV corresponds to the oxygenated adsorbed species. In the same way, the Li 1s core peaks (Figure S3) located at 54.3 eV is associated to the lithium in the spinel structure.

The atomic percentages are gathered in Table 1. The stoichiometry of the spinel surface determined from XPS core peaks are $Li_{1.25}Mn_{1.95}O_{2.97}$ and $Li_{1.04}Mn_{1.90}O_{3.2}$ respectively for x = 0.05 and x = 0.10. The oxygen content is underestimated as the determination of the stoichiometry is based only on the contribution of oxide anion (529.7 eV). Thus, oxygen atoms coordinated to Mn and engaged in surface hydroxyl groups or undercoordinated belong to the component at

531.5 eV. It may be noted a slight deviation of the Li content from the nominal stoichiometry at the surface. The Li/Mn ratio is substantially for the x = 0.05 material larger than expected from nominal values (0.64 and 0.55 against 0.54 and 0.58 for, respectively, x = 0.05 and 0.1).

Nonetheless, the XPS results are consistent with the manganese valence values expected from XRD results, corresponding to a slight increase of the Mn^{4+} concentration (44% in the $Li_{1.05}Mn_{1.95}O_4$ and 46% in the $Li_{1.10}Mn_{1.90}O_4$ vs. 56% and 63%). The discrepancy between the XPS and nominal stoichiometry is associated to the depth of the XPS analysis (5 nm at most) and thus reflects usual surface effects.

3.2.2. After SO_2 adsorption

For the adsorbed materials, the atomic percentages obtained from XPS analyses are gathered in Table 2.

	x = 0.05		x = 0.10	
	B.E. (eV)	**At. %**	**B.E. (eV)**	**At. %**
Mn $2p_{3/2}$	642.3	18.7	642.3	13.5
O 1s	529.9	30.9	529.8	23.3
	531.5	13.2	531.6	19.6
		44.1		42.8
C 1s	284.8	20.9	284.1	24.9
	286.3	2.6	285.7	4.3
	288.0	0.2	287.6	0.4
	288.6	0.6	288.1	2.3
		24.3		31.9
S $2p_{3/2}$	168.5	0.9	168.4	2.2
	169.3	0.4		
		1.3		2.2
Li 1s	54.2	11.6	54.0	9.5

Table 2. Binding energies and atomic percentages determined from XPS analysis for the $Li_{1+x}Mn_{2-x}O_4$ materials after SO_2 adsorption.

The stoichiometry of the surface (considering the Li/Mn ratio) is not impacted by the adsorption for the nominal composition x= 0.05 as we have found a material stoichiometry of $Li_{1.21}Mn_{1.95}O_{3.22}$. For x= 0.01, the stoichiometry of $Li_{1.33}Mn_{1.90}O_3$ corresponds to an increase of the Li/Mn ratio (0.7 after adsorption instead of 0.55 before).

First, we consider the S 2p spectra associated to the sulfur issued from the SO_2 gas probe, Figure 3. Due to the spin orbit coupling, the S 2p core peaks consist of two main components, S $2p_{3/2}$ and S $2p_{1/2}$ separated by 1.2 eV and with an area ratio of 2:1. The S 2p spectra evidence that

the adsorbed species are different for the two spinel materials. The S 2p spectrum of $Li_{1.10}Mn_{1.90}O_4$ can be decomposed into one doublet for which the S $2p_{3/2}$ B.E. value is 168.4 eV. In the case of the $Li_{1.05}Mn_{1.95}O_4$ material, two doublets are needed to fit the experimental spectrum, with an S $2p_{3/2}$ B.E. of 168.5 and 169.3 eV. Based on previous studies[7,10,18], the expected B.E. values of the S $2p_{3/2}$ components after SO_2 adsorption are 167 eV and 169 eV, respectively, in the case of the formation of sulfite and sulfate species at the materials surface. In this study, the B.E.s of the S $2p_{3/2}$ components are slightly larger. Moreover, Flahaut *et al*.[17] have reported an S $2p_{3/2}$ B.E. of 167.9 eV and 169.6 eV for the dipropylsulfate and dimethylsulfite, respectively. Thus, we can suggest that the SO_2 gas probe is adsorbed as sulfite at the $Li_{1.10}Mn_{1.90}O_4$ surface, and both as sulfate and sulfite species for $Li_{1.05}Mn_{1.95}O_4$. The adsorption mechanisms are thus different: a unique acid/base adsorption mode on the $Li_{1.10}Mn_{1.90}O_4$ surface and both acid/base (69%) and redox (31%) modes on the $Li_{1.05}Mn_{1.95}O_4$ surface. Moreover, the concentration of adsorbed species obtained from XPS analyses through the S/Mn ratio, leads to significantly different values, namely 0.1 and 0.2 for $Li_{1.05}Mn_{1.95}O_4$ and $Li_{1.10}Mn_{1.90}O_4$ respectively.

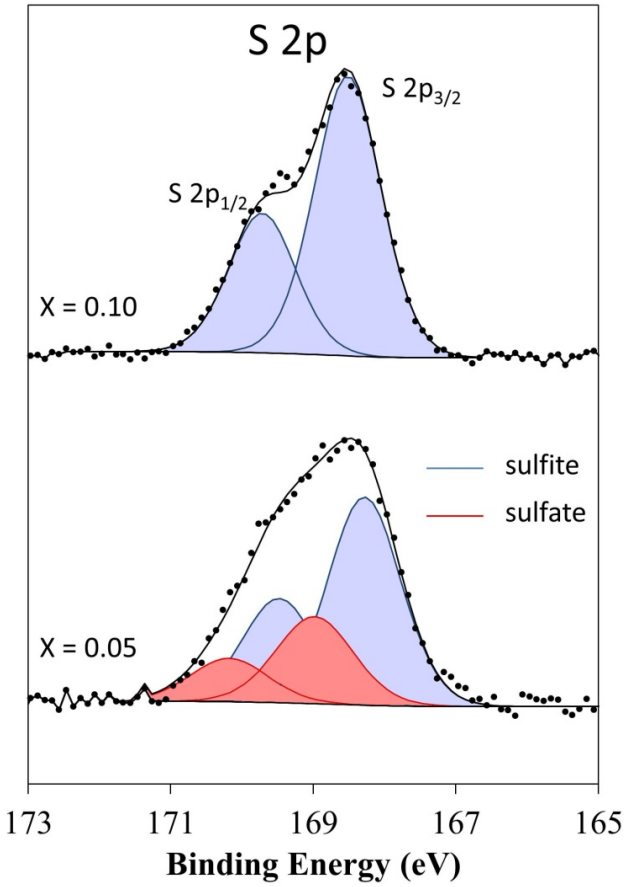

Figure 3. S 2p core peaks after SO_2 adsorption on $Li_{1+x}Mn_{2-x}O_4$ materials with x = 0.10 (top panel) and x = 0.05 (bottom panel).

The O 1s spectra exhibits a significant rise of the component located at 531.5 eV (Figure 2b.) upon adsorption. Moreover, the area ratio between the oxygen components associated to adsorbed species and to oxygen anions of the material is higher for x = 0.10 which is consistent with the difference in the adsorbed species concentrations obtained from the S/Mn ratios (S/Mn ratio = 0.1 and 0.2 for $Li_{1.05}Mn_{1.95}O_4$ and $Li_{1.10}Mn_{1.90}O_4$, respectively).

In contrast, no significant difference (considering the whole envelope shape, components B.E., and FWHM values) can be observed in the Mn 2p spectra as well as for the Mn 3p and Mn 3s

spectra after SO_2 adsorption for the two $Li_{1+x}Mn_{2-x}O_4$ materials. Looking at the spectra more closely, we can detect tiny variations of the manganese spectra after adsorption for the $Li_{1.05}Mn_{1.95}O_4$. First, the determination of the manganese valence from the Mn 2p core peaks highlights an interesting evolution of the manganese electronic structure versus SO_2 adsorption for this composition. The manganese valence has decreased only slightly; 60 ± 1% of the Mn 2p signal is assigned to Mn^{3+} after adsorption instead of 56 ± 1% before adsorption. This result reveals that the redox adsorption mode induces an electronic transfer between the SO_2 gas probe and the Mn^{4+} present at the surface for the x = 0.05 material. In contrast, this effect does not appear in the XPS spectra for the x=0.10 material.

3.3. Computational results

In order to analyze more deeply the electronic processes associated to the surface reactivity, a computational study of the bare surfaces of $LiMn_2O_4$ was undertaken, followed by SO_2 adsorption on various surfaces of $LiMn_2O_4$. Computational accuracy was first checked on the bulk properties of an ideal $LiMn_2O_4$ crystal, depicted in Figure 4a. The calculated value of the lattice parameter is a = 8.427 Å in good agreement with the experimental one[30] of 8.251 Å with a relative deviation of 2%. The magnetic moment calculated on manganese for a ferromagnetic arrangement is 3.8 $\mu_{B,}$ corresponding to a Mn^{3+}/Mn^{4+} mixed valence state for manganese in good agreement with the mixed valence state observed from XPS measurement, and with the 50% Mn^{3+}/50% Mn^{4+}state in this compound.

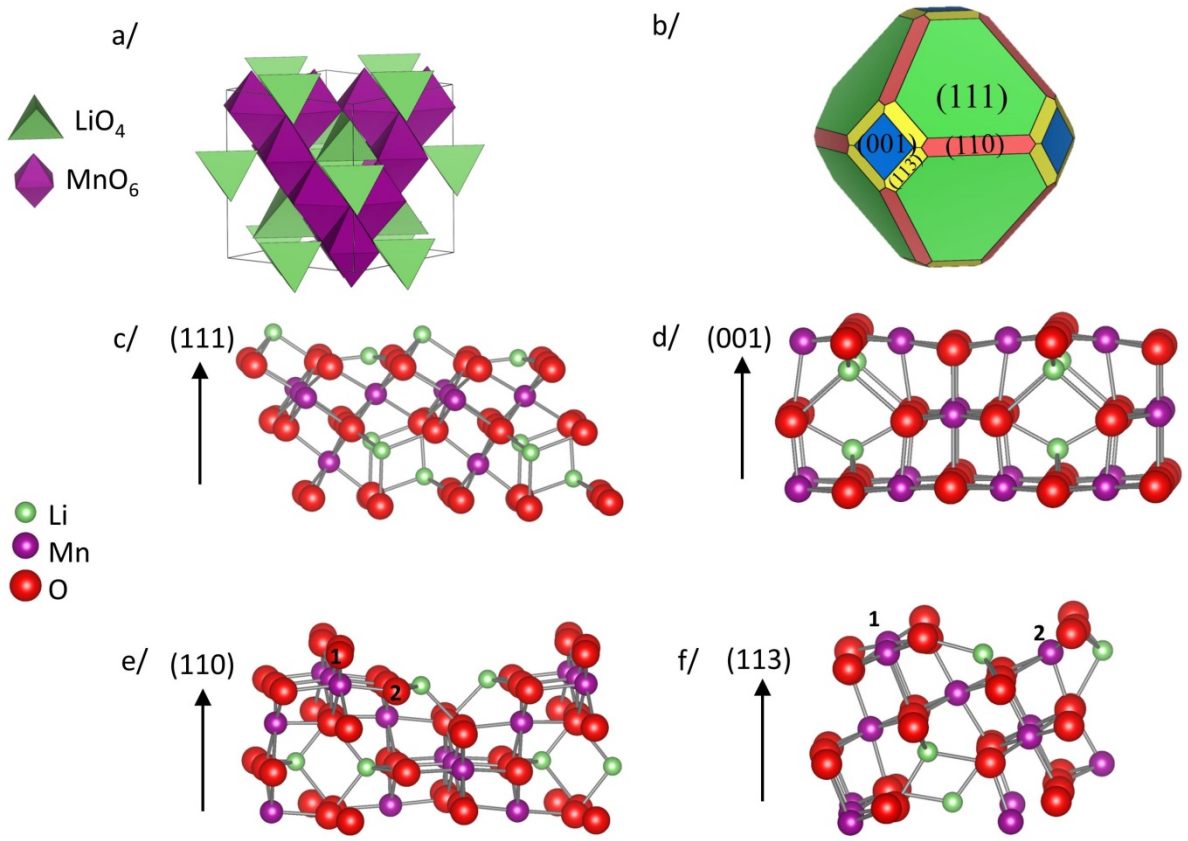

Figure 4. (a) bulk structure of an ideal $LiMn_2O_4$ structure. LiO_4 tetrahedra are in green and MnO_6 octahedra in purple, (b) particles shape representation; (c-f) side views of the first atomic layers of the surface models used in the calculations: (c) (111) surface, (d) (001) surface, (e) (110) surface and (f) (113) surface. Li, Mn and O atoms are in green, purple and red respectively. In figures (e) and (f), the numbers are labelleds used in the main text.

3.3.1. Bare surfaces

We considered the surfaces observed in the truncated octahedron (Figures 1b and 1d) which are assumed to be (111), (001), (110) and (113) as suggested by Kim *et al.*[25]. Following the work of Warburton *et al.*[31] who investigated the surface stability of $LiMn_2O_4$ in various

thermodynamics conditions, we selected the more relevant slab models for each surface on the basis of the thermodynamic stability in a broad range of electrochemical conditions. The selected models are depicted in Figure 4c-4f. Warburton *et al.*[31] showed that the surface formation energies of the (110) and (113) surfaces are higher than those of the (111) and (001) surfaces. These results are consistent with the shape of the particles we obtained (Figures 1b and 1d) where the (111) and (001) surfaces exhibit the largest area.

The (111) surface model, called Li-rich model by Warburton *et al.*[31] (Figure 4c) is terminated by a lithium layer which enhances the surface stability. This lithium layer is stacked on top of a sheet of MnO_6 octahedra. The computed magnetic moments of the manganese atoms in the sub-surface layer are 3.3 μ_B for 2/3 of the manganese atoms, and 3.9 μ_B for 1/3 of the manganese atoms, corresponding to Mn^{4+} and Mn^{3+} species respectively, according to the calculations on the reference compounds (see Supporting Information, Table S1).

The (001) surface model, called Mn/O (001) by Warburton *et al.*[31] (Figure 4d) is the most stable among the (001) surface composition on a broad range of thermochemical conditions (oxidizing conditions and electrode potential versus Li^+/Li potential). It consists in a stacking of Mn_2O_4 and Li layers, the termination layers being an Mn_2O_4 sheet with manganese atoms in an ML_5 environment. The computed magnetic moments of manganese atoms on the surface layer are 4.0 μ_B, and correspond to Mn^{3+} species. From the top to the core of the slab model, the computed magnetic moments are 3.4 μ_B, 3.6 μ_B and 3.8 μ_B which is the bulk value, corresponding to an increasing content in Mn^{3+}.

The (110) surface model, called Li/O (110) by Warburton *et al.*[31] (Figure 4e) follows a stacking sequence of alternate $LiMnO_2$ and MnO_2 layers with oxygen atoms on the last atomic

layer. This oxygen layer completes the manganese octahedra at the surface, leading to an enhanced stability. The magnetic moments of the sub-surface manganese atoms are 3.3 μ_B, corresponding to Mn^{4+}. As already observed for the (001) surface model, from the top to the core of the slab model, the computed magnetic moments increase corresponding to an increasing proportion of Mn^{3+} species. The oxygen atoms of the last atomic layer, label 1 in Figure 4e, exhibit a lower electronic charge of -0.76 e instead of -1.07 e in the bulk of $LiMn_2O_4$. This is attributed to the low coordination of these oxygen atoms which present only two cation neighbors instead of four in the bulk structure.

The (113) surface model, called Li/Mn/O by Warburton *et al*.[31] (Figure 4f) is considered as a high-index surface and can be described as a stacking of Mn_2O_4 and Li layers, as the (001) surface, but twisted around an in-plane axis by about 45°. At the surface layer, this leads to manganese atoms in an ML_5 environment which exhibit magnetic moments of 4.0 μ_B for 2/3 of the manganese atoms (label 1, Figure 4f), and 2.8 μ_B for 1/3 of the manganese atoms (label 2, Figure 4f), corresponding to Mn^{3+} and Mn^{4+} respectively.

The four models described above present various oxidation states for the manganese atoms on the last surface layers and therefore suggest different behaviors upon adsorption of a gas probe. The variety of the considered models will allow us to establish the relationship between the chemical composition and the surface reactivity.

3.3.2. Surfaces after SO_2 adsorption

Calculations of the adsorption of an SO_2 probe molecule were performed on the four surface models described above. Sulfite and sulfate sites were probed in an exhaustive way by considering all nonequivalent oxygen atoms at the last atomic layer of the surface. The initial

geometries were obtained by placing the SO_2 molecule either in a tetrahedral (bridge sites) or a trigonal (top sites) environment for the sulfur atom leading to the formation of sulfate or sulfite species, respectively. For the sulfite adsorption, the sulfur atom is located 1.55 Å away from the oxygen atom belonging to the surface. For the sulfate adsorption, the sulfur atom is located initially 1.55 Å away from the barycenter of two surface oxygen atoms. The geometry is then fully relaxed and the adsorption energy, E_{ads}, is computed from

$$E_{ads} = E_{surface+SO_2} - (E_{surface} + E_{SO_2})$$

where $E_{surface+SO_2}$ is the energy of the adsorbed system, $E_{surface}$ is the bare surface energy and E_{SO_2} the energy of an isolated SO_2 molecule obtained from the calculation of an isolated SO_2 molecule in a cubic box of 10 Å length. The adsorption energies and the electronic transfers, from the SO_2 molecule towards the surface, of the most stable sulfite and sulfate adsorptions are gathered in Table 3. The electronic transfers were computed from the Bader charges analysis.

Surface	**species**	**E_{ads} (eV)**	**Δq_{SO_2}**
(111)	Sulfite	-1.12	-0.4
(001)	Sulfite	-1.49	-0.1
(110)	Sulfite	-0.89	-0.2
(110)	Sulfate	-2.71	1.1
(113)	Sulfite	-1.14	-0.4
(113)	Sulfate	-4.29	1.0

Table 3. Adsorption energy (E_{ads}) and electronic transfer, Δq, from SO_2 towards the surface for the most stable structures.

Whatever the surface, the electronic transfer is about one electron from the SO_2 molecule toward the surface in the case of the formation of sulfate species, while a smaller transfer, of at most 0.4 electron from the surface toward the SO_2 molecule, is obtained in the case of sulfite species. This agrees with the redox reactivity associated with the sulfate formation and the acid-base reactivity associated with the formation of sulfite species[8,9]. The range of computed adsorption energies indicates the formation of chemisorbed species, stable enough to be observed by XPS characterizations under ultra-high vacuum conditions.

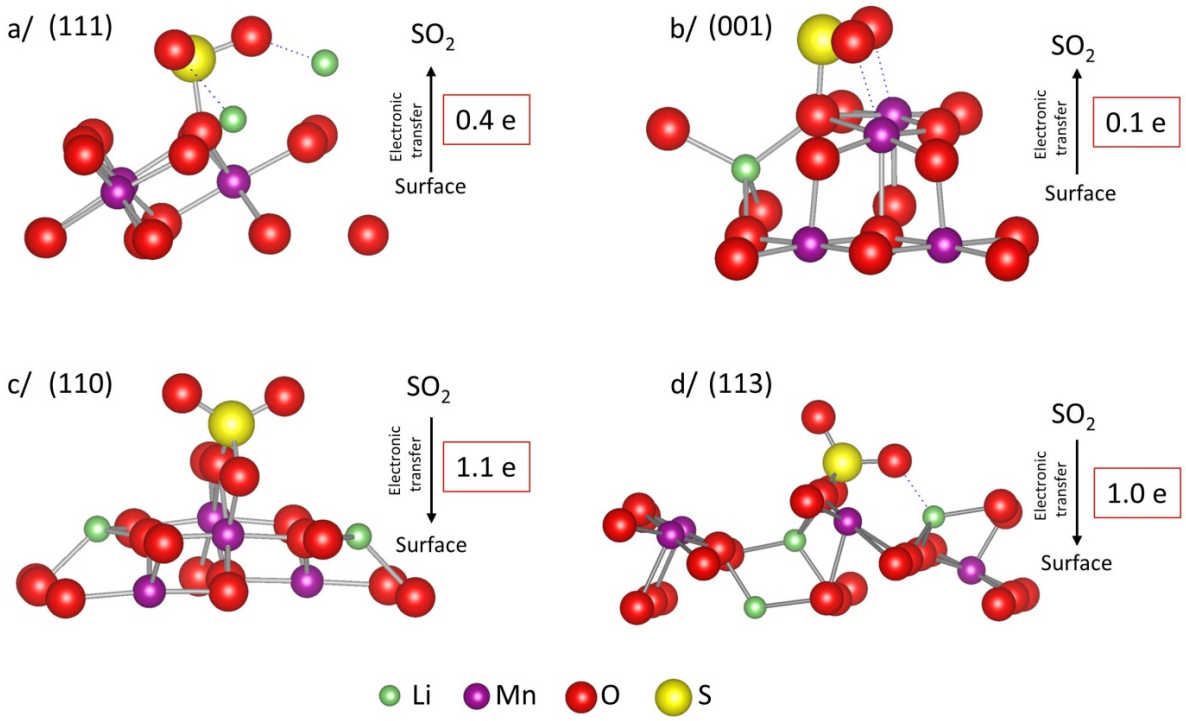

Figure 5. SO_2 adsorption on $LiMn_2O_4$ surfaces after structural relaxation. (a) and (b) Sulfite adsorption mode on (111) and (001) surfaces respectively, (c) and (d) sulfate adsorption mode on (110) and (113) respectively.

In the case of the (111) and (001) surfaces, the formation of sulfite species is favored with an adsorption energy of -1.12 and -1.49 eV respectively. The formation of sulfate species was also considered but actually leads to the formation of sulfite species. The relaxed geometries of the most stable adsorptions are depicted in Figure 5a and Figure 5b for surfaces (111) and (001) respectively. In both cases, the adsorbed molecule is stabilized by the formation of secondary interactions between oxygen atoms of SO_2 and cations of the last atomic layer of the surface. In the case of the (001) surface, the oxygen atoms of SO_2 complete the coordination sphere of the manganese atoms in order to place them in an ML_6 environment corresponding to the bulk structure. The lengths of these bonds are similar to other Mn-O bonds in the bulk octahedra (2.03/2.14 Å vs 1.96 Å). For both surfaces, the electronic structure of manganese atoms is kept unchanged, consistently with the low charge transfer associated to the acid-base reactivity and the formation of sulfite species.

In the case of the (110) and (113) surfaces, the formation of sulfate species is favored although the formation of sulfite species appears thermodynamically possible. On the (113) surface the formation of sulfate species is obtained only in the vicinity of the Mn^{4+} manganese atoms, label 2 in Figure 4f. The most stable structure is depicted in Figure 5d and the associated adsorption energy is -4.29 eV. The electronic transfer from the SO_2 molecule toward the surface involves a large rise in the magnetic moment of the closest manganese atom from 2.77 to 4.68 μ_B. This can be interpreted as the reduction $Mn^{4+} + 2e^- \rightarrow Mn^{2+}$ and as a transfer of formally two electrons from the SO_2 molecule as already observed in a previous study on $LiMO_2$ compounds[9]. In addition, the SO_2 molecule is stabilized by the formation of secondary interaction with a free lithium atom at the surface (interatomic distance 1.9 Å), materialized by a dashed bond in Figure 5d, leading to a strong adsorption. On the (110) surface, the most stable sulfate species is

obtained by an adsorption on the last oxygen layer, label 1 in Figure 4e and is depicted in Figure 4c. The electronic transfer from the SO_2 molecule toward the surface is spread over both the oxygen atoms of the last atomic layer and one sub-surface manganese. Indeed, the electronic structure analysis leads to a reduction of one sub-surface manganese atom from Mn^{4+} to Mn^{3+} which is evidenced by a rise in magnetic moments from 3.31 to 3.99 μ_B. Simultaneously, the electronic charges of oxygen atoms on top of which the adsorption takes place decrease form -0.76e to -1.12e.

In conclusion, the formation of sulfate species, which involves the reduction of species on the last atomic layers, is favored only if Mn^{4+} species are available on top of the surface, namely for the (110) and (113) surfaces. On the contrary, if only Mn^{3+} species are available or Mn^{4+} are buried in the sub-surface layer, the formation of sulfite species is favored which is the case for the (111) and (001) surfaces. In addition, this conclusion can be reinforced by our previous work[9] on $LiMnO_2$ where only sulfite species were obtained when the last atomic layer contains only Mn^{3+} cations (the (104) surface) and both sulfate and sulfite species were obtained when higher oxidation degrees are present for manganese present at the surface (Mn^{4+} and Mn^{2+} on the (110) surface).

4. DISCUSSION

The two spinel materials studied in this paper differ in their nominal Li/Mn ratio, $Li_{1.05}Mn_{1.95}O_4$ and $Li_{1.1}Mn_{1.90}O_4$. The slight decrease in the lattice parameter with the increasing Li/M ratio is consistent with the increase of the Mn valence. Nonetheless, the Li/Mn ratio is different on the surface and in the bulk of the materials, which leads to surface stoichiometries determined by XPS of $Li_{1.2\pm0.3}Mn_{1.95}O_{3.0\pm0.1}$ and $Li_{1.0\pm0.3}Mn_{1.9}O_{3.2\pm0.1}$ for x = 0.05 and x = 0.10 respectively showing

that the presence of trivalent manganese (Mn^{3+}) at the surface is larger than expected theoretically.

The secondary electron micrographs obtained on theses samples show that only the (111), (001) and (110) surfaces have been experimentally identified for the truncated octahedral particles in good agreement with the spinel structure. Thus, we discuss only of those three surfaces from a theoretical and experimental point of view.

According to the calculations on the (111), (110) and (001) surface orientations, the manganese cations are only present in the Mn^{3+} and Mn^{4+} oxidation state. The manganese cations, which are located at the sub-surface layer of the (111) orientation, possesses a $Mn^{3+/4+}$ mixed valence. For the other two orientations, the manganese cations at the extreme surface exhibit a unique valence, Mn^{3+} for the (001) and Mn^{4+} for the (110) orientation. In a same manner, the valence of the manganese has been clearly identified by XPS and in particular by combining the information issued from the Mn 2p and Mn 3s core peaks spectra and corresponds to a $Mn^{3+/4+}$ mixed valence. As the SEM study strongly suggests a majority of (111) and (001) surfaces, XPS results and theoretical calculations are in accordance to propose a mixed valency of the manganese cations at the spinel surface.

After SO_2 adsorption on the three considered orientations, computational results evidence the formation of either sulfite or sulfate species. Only sulfite species are thermodynamically stable on the (111) and (001) surfaces, whereas both sulfite and sulfate species can be obtained on the (110) surface with a higher stability of sulfate species.

Concurrently, the adsorbed species have also been experimentally characterized by XPS after gas probe adsorption on the material surface. From the S 2p core peaks, we have identified a sole

sulfite adsorption mode for the $Li_{1.1}Mn_{1.90}O_4$ spinel, while both sulfate and sulfite species were obtained in the case of the $Li_{1.05}Mn_{1.95}O_4$ spinel with sulfite species in higher quantity.

According to computational results, the sulfate species detected for the x = 0.05 spinel material could only be linked to the redox reactivity of the (110) surfaces of the spinel crystals. Two experimental results substantiate the assignment of the redox reactivity to the (110) surfaces: 1) the (110) surfaces are present in a lesser amount than (111) and (110) and, 2) the acid-base adsorption mode is predominant (69% of sulfite compared to 31% of sulfate species). In consequence, although the amount of the different orientations was not quantified accurately, we may suggest that the difference in the reactivity of the x = 0.1 and x = 0.05 samples is due to a morphology change leading to a higher amount of (110) surface in the x = 0.05 sample than x = 0.1 which can be observed from SEM imaging, Figure 2.

This argumentation, based on computational results, is strengthened by the full agreement with the description of the electronic processes taking place, analyzed from the XPS measures. Indeed, computational results evidence a large electronic transfer, associated to the reduction of surface or sub-surface manganese atoms, in the case of the formation of sulfate species, while only low transfers are obtained in the case of the formation of sulfite species, these two processes being associated to a redox or an acid-base reactivity, respectively. Moreover, in the case of sulfate formation on the (110) surfaces, the calculations show that the closest manganese atoms are reduced from Mn^{4+} to Mn^{3+}. From XPS analysis of the Mn 2p spectra decomposition after SO_2 adsorption, a noticeable increase of the Mn^{3+} content (from 56 ± 1% to 60 ± 1%) has been observed, in the case of $Li_{1.05}Mn_{1.95}O_4$ material. This indicates a reduction of Mn^{4+} into Mn^{3+} associated to the redox adsorption process. For the $Li_{1.1}Mn_{1.90}O_4$ spinel, no change in the oxidation state of the manganese cation has been experimentally detected which agrees with the

acid-base character of the sulfite adsorption suggested from computational and experimental results.

5. CONCLUSION

In this work, we focus on the surface reactivity of $Li_{1+x}Mn_{2-x}O_4$ spinel materials with two different stoichiometries (x = 0.05 and x = 0.10). Their structure, morphology and chemical composition were characterized in-depth. The surface reactivity was investigated through the adsorption of a gaseous probe (SO_2) in controlled conditions, and both XPS analyses and first-principle calculations were undertaken in order to identify and quantify the adsorbed species on the surface and characterize the surface reactivity.

The formation of both sulfite and sulfate species, associated to an acid-base and redox reactivity, respectively, was identified from XPS analysis and computational results. Both approaches allow us to evidence that the formation of sulfate species is only allowed in the presence of Mn^{4+} cations which are reduced due to an electronic transfer from the SO_2 molecule to the surface of the material. On the contrary, only sulfite species are formed in the presence of Mn^{3+} cations. More generally for manganese compounds, increasing the presence of manganese atoms at the +III oxidation degree limits the redox surface reactivity.

According to the computational and experimental results, the presence of sulfate species could be attributed to the (110) facets in the spinel crystals. In consequence, we may suggest that the reactivity of manganese materials can be controlled by managing the shape of the crystal. Indeed, redox reactivity could be limited in the case of spinel compounds by lowering the area of (110) facets or more generally by lowering the amount of manganese species at high oxidation degree.

It would be worthy of continuing research and investigations in order to characterize the proportion of each surface in the two spinel materials. Thus, we would precise the link between the morphology and the reactivity of the spinel materials.

ASSOCIATED CONTENT

Supporting Information. Mn 2p, Mn 3s, Mn 3p spectra from X-Ray Photoelectron Spectroscopy analysis are included. Lattice parameters of calculated MnO, Mn_2O_3 and MnO_2 materials and the manganese atoms magnetic moment are resumed. This material is available free of charge via the Internet at http://pubs.acs.org.

AUTHOR INFORMATION

Corresponding Author

*Germain Vallverdu

germain.vallverdu@univ-pau.fr

Present Addresses

CNRS/ Univ Pau & Pays Adour, Institut des Sciences Analytiques et de Physico-chimie pour l'Environnement et les Matériaux, UMR5254, 64000, Pau, France

ACKNOWLEDGMENT

The authors thank the Conseil Général des Pyrénées Atlantiques and the French Research Network on the Electrochemical Energy Storage (RS2E) for funding the AQT's PhD fellowship,

and Christian Masquelier (LRCS-Amiens) for fruitful discussions on the spinel materials $Li_{1+x}Mn_{2-x}O_4$. This project received also funding from Région Nouvelle Aquitaine and the French National Research Agency (STORE-EX Labex Project ANR-10-LABX-76-01). The theoretical calculations were performed using HPC resources from GENCI-CINES (Grant 2017-A0010806920) and the Mesocentre de Calcul Intensif Aquitain (MCIA).

References

(1) Xu, B.; Meng, S. Factors Affecting Li Mobility in Spinel $LiMn_2O_4$ - A First-Principles Study by GGA and GGA+U Methods. *J. Power Sources* **2010**, *195* (15), 4971–4976.

(2) Ozawa, K. Lithium-Ion Rechargeable Batteries with $LiCoO_2$ and Carbon Electrodes: The $LiCoO_2$/C System. *Solid State Ion.* **1994**, *69* (3), 212–221.

(3) Amatucci, G. G.; Pereira, N.; Zheng, T.; Tarascon, J.-M. Failure Mechanism and Improvement of the Elevated Temperature Cycling of LiMn[Sub 2]O[Sub 4] Compounds Through the Use of the $LiAl_xMn_{2-x}O_{4-z}F_z$ Solid Solution. *J. Electrochem. Soc.* **2001**, *148* (2), A171.

(4) Amine, K.; Liu, J.; Belharouak, I.; Kang, S.-H.; Bloom, I.; Vissers, D.; Henriksen, G. Advanced Cathode Materials for High-Power Applications. *J. Power Sources* **2005**, *146* (1–2), 111–115.

(5) Hunter, J. C. Preparation of a New Crystal Form of Manganese Dioxide: λ-MnO 2. *J. Solid State Chem. Fr.* **1981**, *39*, 142–147.

(6) Gummow, R. J.; de Kock, A.; Thackeray, M. M. Improved Capacity Retention in Rechargeable 4 V Lithium/Lithium-Manganese Oxide (Spinel) Cells. *Solid State Ion.* **1994**, *69* (1), 59–67.

(7) Andreu, N.; Flahaut, D.; Dedryvère, R.; Minvielle, M.; Martinez, H.; Gonbeau, D. XPS Investigation of Surface Reactivity of Electrode Materials: Effect of the Transition Metal. *ACS Appl. Mater. Interfaces* **2015**, *7* (12), 6629–6636.

(8) Andreu, N.; Baraille, I.; Martinez, H.; Dedryvère, R.; Loudet, M.; Gonbeau, D. New Investigations on the Surface Reactivity of Layered Lithium Oxides. *J. Phys. Chem. C* **2012**, *116* (38), 20332–20341.

(9) Vallverdu, G.; Minvielle, M.; Andreu, N.; Gonbeau, D.; Baraille, I. First Principle Study of the Surface Reactivity of Layered Lithium Oxides $LiMO_2$ (M = Ni, Mn, Co). *Surf. Sci.* **2016**, *649*, 46–55.

(10) Dahéron, L.; Dedryvère, R.; Martinez, H.; Flahaut, D.; Ménétrier, M.; Delmas, C.; Gonbeau, D. Possible Explanation for the Efficiency of Al-Based Coatings on $LiCoO_2$: Surface Properties of $LiCo_{1-x}Al_xO_2$ Solid Solution. *Chem. Mater.* **2009**, *21* (23), 5607–5616.

(11) Masquelier, C.; Tabuchi, M.; Ado, K.; Kanno, R.; Kobayashi, Y.; Maki, Y.; Nakamura, O.; Goodenough, J. B. Chemical and Magnetic Characterization of Spinel Materials in the $LiMn_2O_4$–$Li_2Mn_4O_9$–$Li_4Mn_5O_{12}$ System. *J. Solid State Chem.* **1996**, *123* (2), 255–266.

(12) Bianchini, M.; Fauth, F.; Suard, E.; Leriche, J.-B.; Masquelier, C.; Croguennec, L. Spinel Materials for Li-Ion Batteries: New Insights Obtained by Operando Neutron and Synchrotron X-Ray Diffraction. *Acta Crystallogr. Sect. B Struct. Sci. Cryst. Eng. Mater.* **2015**, *71* (6), 688–701.

(13) Bianchini, M.; Suard, E.; Croguennec, L.; Masquelier, C. Li-Rich $Li_{1+x}Mn_{2-x}O_4$ Spinel Electrode Materials: An Operando Neutron Diffraction Study during Li^+ Extraction/Insertion. *J. Phys. Chem. C* **2014**, *118* (45), 25947–25955.

(14) Shannon, R. D. Revised Effective Ionic Radii and Systematic Studies of Interatomic Distances in Halides and Chalcogenides. *Acta Crystallogr. A* **1976**, *32* (5), 751–767.

(15) Brunauer, S.; Emmett, P. H.; Teller, E. Adsorption of Gases in Multimolecular Layers. *J. Am. Chem. Soc.* **1938**, *60* (2), 309–319.

(16) Lindberg, B. J.; Hamrin, K.; Johansson, G.; Gelius, U.; Fahlman, A.; Nordling, C.; Siegbahn, K. Molecular Spectroscopy by Means of ESCA II. Sulfur Compounds. Correlation of Electron Binding Energy with Structure. *Phys. Scr.* **1970**, *1* (5–6), 286–298.

(17) Flahaut, D.; Minvielle, M.; Sambou, A.; Lecour, P.; Legens, C.; Barbier, J. Identification of Sulphur, Oxygen and Nitrogen Species in Heavy Oils by X-Ray Photoelectron Spectroscopy. *Fuel* **2017**, *202* (Supplement C), 307–317.

(18) Guimon, C.; Gervasini, A.; Auroux, A. XPS Study of the Adsorption of SO_2 and NH_3 over Supported Tin Dioxide Catalysts Used in De-NOx Catalytic Reaction. *J. Phys. Chem. B* **2001**, *105* (42), 10316–10325.

(19) Kresse, G.; Furthmüller, J. Efficient Iterative Schemes for Ab Initio Total-Energy Calculations Using a Plane-Wave Basis Set. *Phys. Rev. B* **1996**, *54* (16), 11169–11186.

(20) Kresse, G.; Hafner, J. Ab Initio. *Phys. Rev. B* **1994**, *49* (20), 14251–14269.

(21) Kresse, G.; Joubert, D. From Ultrasoft Pseudopotentials to the Projector Augmented-Wave Method. *Phys. Rev. B* **1999**, *59* (3), 1758–1775.

(22) Perdew, J. P.; Chevary, J. A.; Vosko, S. H.; Jackson, K. A.; Pederson, M. R.; Singh, D. J.; Fiolhais, C. Atoms, Molecules, Solids, and Surfaces: Applications of the Generalized Gradient Approximation for Exchange and Correlation. *Phys. Rev. B* **1992**, *46* (11), 6671–6687.

(23) Perdew, J. P.; Wang, Y. Accurate and Simple Analytic Representation of the Electron-Gas Correlation Energy. *Phys. Rev. B* **1992**, *45* (23), 13244–13249.

(24) Dudarev, S. L.; Botton, G. A.; Savrasov, S. Y.; Humphreys, C. J.; Sutton, A. P. Electron-Energy-Loss Spectra and the Structural Stability of Nickel Oxide: An LSDA+U Study. *Phys.*

Rev. B **1998**, *57* (3), 1505–1509.

(25) Henkelman, G.; Arnaldsson, A.; Jónsson, H. A Fast and Robust Algorithm for Bader Decomposition of Charge Density. *Comput. Mater. Sci.* **2006**, *36* (3), 354–360.

(26) Tang, W.; Sanville, E.; Henkelman, G. A Grid-Based Bader Analysis Algorithm without Lattice Bias. *J. Phys. Condens. Matter* **2009**, *21* (8), 084204.

(27) Kim, J.-S.; Kim, K.; Cho, W.; Shin, W. H.; Kanno, R.; Choi, J. W. A Truncated Manganese Spinel Cathode for Excellent Power and Lifetime in Lithium-Ion Batteries. *Nano Lett.* **2012**, *12* (12), 6358–6365.

(28) Allen, G. C.; Harris, S. J.; Jutson, J. A.; Dyke, J. M. A Study of a Number of Mixed Transition Metal Oxide Spinels Using X-Ray Photoelectron Spectroscopy. *Appl. Surf. Sci.* **1989**, *37* (1), 111–134.

(29) Brabers, V. A. M.; van Setten, F. M.; Knapen, P. S. A. X-Ray Photoelectron Spectroscopy Study of the Cation Valencies in Nickel Manganite. *J. Solid State Chem.* **1983**, *49* (1), 93–98.

(30) Berg, H.; Thomas, J. O. Neutron Diffraction Study of Electrochemically Delithiated LiMn2O4 Spinel. *Solid State Ion.* **1999**, *126* (3–4), 227–234.

(31) Warburton, R. E.; Iddir, H.; Curtiss, L. A.; Greeley, J. Thermodynamic Stability of Low- and High-Index Spinel $LiMn_2O_4$ Surface Terminations. *ACS Appl. Mater. Interfaces* **2016**, *8* (17), 11108–11121.

Table of Contents Graphic